# Veröffentlichung



**Autoren**

Müller, Lars;Kozulovic, Dragan;Hepperle, Martin;Radespiel, Rolf

**Titel**

The Influence of the Propeller Position on the Aerodynamics of a Channel Wing

**Publisher o. Konferenz**

Proc. of 61. Deutscher Luft- und Raumfahrtkongress, No. DLRK 2012-281259, Berlin (Germany)

**Jahr**

2012

**Internet-Link (Doi-Nr.)**

# THE INFLUENCE OF THE PROPELLER POSITION ON THE AERODYNAMICS OF A CHANNEL WING

L. Müller*, D. Kožulović*, M. Hepperle†, R. Radespiel*

*Technische Universität Braunschweig, Institute of Fluid Mechanics,
Hermann-Blenk-Strasse 37, 38108 Braunschweig

† Deutsches Zentrum für Luft- und Raumfahrt, Institute of Aerodynamics and Flow Technology,
Lilienthalplatz 7, 38108 Braunschweig

**Abstract**

The paper investigates a generic channel wing configuration regarding the aerodynamic sensitivities to design parameters. Numerical simulations include a variation of the channel depth, the chordwise position of the propeller and clearance for the simplified wing and actuator disk geometry. Evaluation of the lift-to-drag ratio of the wing and the propeller efficiency indicate complex dependencies between geometric parameters and aerodynamic performance. It is evident that a highly integrated design with large embedding depth and minimum gap size leads to most beneficial influences on the wing but an adverse effect on the propeller. As the propulsion system always suffers from this kind of installation, the mutual influence is not of synergistic nature. Evaluating a corrected lift-to-drag ratio which takes the thrust loss on the actuator disk into account, the figure of merit of the overall configuration is only little affected by the three design parameters. More specifically, a less close coupling is considered advantageous when aiming at high climb angles. Together with the expected shielding capabilities, a small noise footprint at take-off can be indirectly achieved through aerodynamically driven measures.

## Nomenclature

| | |
|---|---|
| $b$, $s$ | wing span, semispan |
| $c$ | chord length |
| $c_l$, $c_d$ | local lift, drag coefficients |
| $c_\mu$ | jet momentum coefficient |
| $C_T$ | aircraft thrust coefficient |
| $d$ | gap between propeller tip and wing surface |
| $D_P$ | propeller diameter |
| $D$, $C_D$ | drag, drag coefficient of aircraft |
| $L$, $C_L$ | lift, lift coefficient of aircraft |
| Ma | Mach number |
| $n$ | propeller shaft speed |
| $p$, $c_p$ | static pressure, pressure coefficient |
| $P_S$, $C_{P,s}$ | propeller shaft power, power coefficient |
| $q_\infty$, $\rho_\infty$ | dynamic pressure, density (free-stream) |
| Re | Reynolds number |
| $S_{ref}$ | wing area of reference aircraft |
| $T$, $t/t_{max}$ | thrust of one engine, relative local thrust |
| $V$ | flow velocity |
| $W$ | aircraft take-off weight |
| $x$, $y$, $z$ | Cartesian coordinates |
| $y^+$ | dimensionless wall coordinate |
| $\alpha$ | angle of attack (AOA) |
| $\alpha_e$ | effective angle of attack at blade element |
| $\eta_P$, $\eta_{Pro}$ | propeller efficiency, propulsive efficiency |
| $\theta$ | climb angle |

*Subscripts*

| | |
|---|---|
| *inst* | installed (thrust) |
| *isol* | isolated (thrust) |
| *j* | jet (at nozzle exit) |

## 1. INTRODUCTION

Believing the recent air traffic forecasts, the world-wide amount of revenue passenger kilometres (RPK) will grow by about 5 % per year [1]. It is estimated for Europe that the number of hub-airports will double until 2030 while the existing hubs have to cope with additional load. In fact, many large European airports are already operating at their capacity limit as airport extensions are not accepted by the local population or simply not possible due to the space requirements. In order to relieve the hub-and-spoke system, additional point-to-point connections can be established from and to smaller airports. Commercial operation with single-aisle airliners from short runways will require a *short take-off and landing* (STOL) concept that addresses noise and carbon dioxide emissions. To achieve the goal of a quiet and efficient STOL aircraft, related technologies such as active flow control are currently under investigation in the collaborative research centre SFB 880 (funded by Deutsche Forschungsgemeinschaft DFG).

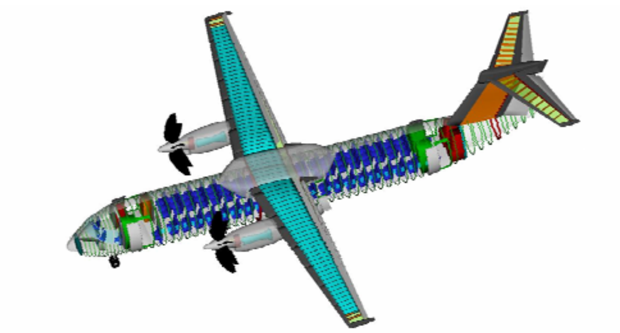

FIGURE 1. Baseline design of commercial STOL aircraft.

The baseline version of a short-haul demonstrator for 100 passengers was developed by means of preliminary aircraft design considering the (academic) technology level of 2011 (FIGURE 1). For maximum take-off performance and efficiency at cruise, a turboprop engine was selected to deliver the required thrust. The key parameters of this reference aircraft are given in TAB 1.

| | |
|---|---|
| Payload | 12000 kg (100 PAX + freight) |
| Range | 2000 km |
| Take-off distance | < 800 m |
| $C_{L,max}$ (Landing) | 3.4 |
| *T/W* (Take-off) | 0.49 |

TAB 1. Specifications of the STOL aircraft

As noise is an issue for open rotors in general, unconventional propeller installation concepts shall either directly or indirectly lead to an acoustically beneficial configuration. The direct way is to mount the propeller over the wing in order to shield the noise which can be perceived at the ground. On the other hand the aerodynamic performance can be optimized for a given engine power to increase the climb angle

$$\sin\theta = \frac{T}{W} - \frac{1}{L/D} \tag{1}$$

and thus reducing the noise footprint. Regarding the combination of actual thrust and lift-to-drag ratio it was shown by *Müller et al.* [2] that an over-the-wing propeller is superior to a conventional tractor configuration. Furthermore embedding the propeller into the wing would be beneficial to minimize the pitching moment due to thrust. The resulting channel wing configuration is investigated in the present paper in terms of aerodynamic sensitivities. In particular, three geometry parameters, namely the channel depth, the axial position of the propeller as well as the clearance between propeller tip and wing surface are varied. Numerical simulations have been conducted for take-off conditions to reveal the dependencies of the mutual influence between propeller and wing with respect to their positions.

## 2. TEST CASE

### 2.1. Geometry

For simplification reasons, the study was carried out on generic propeller-wing geometries. However, in order to transfer the results to the overall aircraft system, the most important parameters are based on the preliminary design of the reference aircraft. The corresponding profile of the wing section at the spanwise coordinate of the propeller axis ($c$ = 3.8 m) was extruded to an unswept wing with rectangular planform. In order to exclude aspect ratio dependencies and tip vortices, a symmetry condition was applied at both ends. A wing span of $b = 5c$ was chosen to minimize the influence of the propeller reflections. The actual profile is a modified version of the DLR F15 airfoil [3], featuring a 0.25$c$ long plain flap with Coanda type boundary layer control [4], [5]. At the beginning of the cylindrical Coanda-surface, a nozzle blows out a tangential jet which is fed by pressurized air from a plenum. For the flap angle of 45°, a momentum coefficient of

$$c_\mu = \frac{V_j \cdot \dot{m}_j}{q_\infty \cdot S} = 0.03 \tag{2}$$

is adjusted to ensure attached flow at optimum efficiency.

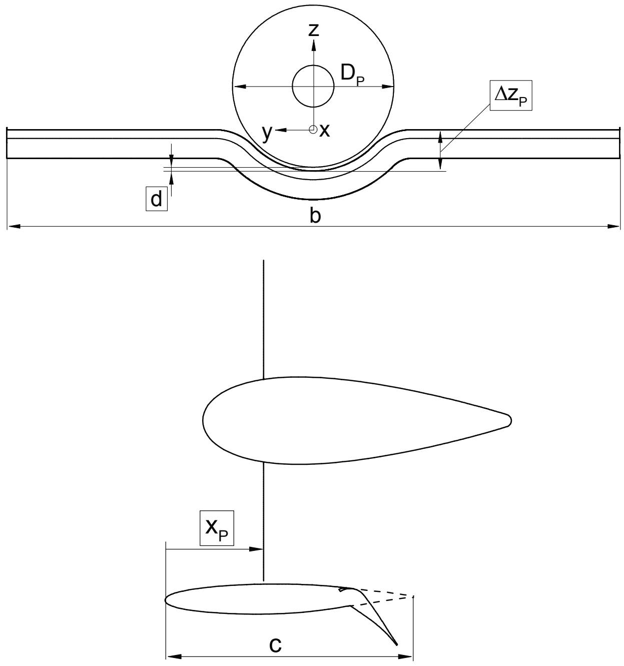


FIGURE 2. Front and side view of channel wing geometry with dimensions. The parameters of the propeller position are highlighted by a box.

The effect of the propulsion system was simulated by using an actuator disk and a generic, rotationally symmetric nacelle. The diameter of the propeller and disk, respectively, is $D_P$ = 5 m = 1.32·$c$ with a hub ratio of 0.258.

### 2.2. Configurations

For this investigation on channel wing design with partially embedded propeller, the following three geometric parameters are varied, cf. FIGURE 2:

- The channel depth $\Delta z_P/D_P$ which can be also understood as propeller embedding depth.
- The axial resp. chordwise position of the propeller $x_P/c$.
- The clearance between blade tip and wing surface, represented by the gap size $d/D_P$.

The baseline configuration is the channel wing of the fundamental study [2] with $\Delta z_P/D_P$ = 1/6, $x_P/c$ = 0.4 and $d/D_P$ = 0.01. For each variant, only one of the three parameters was changed. By this approach it was possible to extract accurate sensitivities of the three-dimensional parameter space with only 10 different configurations. All in all, four channel types $\Delta z_P/D_P$ = {0; 1/6; 1/4; 1/2}, five axial positions $x_P/c$ = {0.1; 0.25; 0.4; 0.55; 0.7} and four gap sizes $d/D_P$ = {0.002; 0.01; 0.02; 0.05} are covered. It is worth mentioning that the clearance was adjusted by the radius of the channel segment rather than the vertical position of the propeller. This allows for a constant gap along a large portion of the channel surface. Furthermore, a radius of $0.25 \cdot D_P$ was applied on the junction between channel and outer wing in order to avoid cross flow-induced separation as well as self-intersection problems of the deflected flap.

### 2.3. Flow Conditions

While the airframe noise is dominant at landing, the propulsion system is the most important noise source at take-off. At this operating point, the aerodynamic influence between propeller and wing is maximum due to the high thrust. For these two reasons, following the fundamental study by *Müller et al.* [2], the take-off condition has been selected for the underlying parameter study. The particular operating point is the first climb segment with a Mach number of $Ma_\infty$ = 0.172, a profile lift coefficient of $c_l$ = 3.1 and a (required) thrust coefficient of

$$c_T = \frac{2 \cdot T}{q_\infty S_{ref}} = 0.783 \tag{1}$$

for the overall aircraft. For the chord length of the profile section at the propeller ($c$ = 3.8 m) the flow is characterized by a Reynolds number of Re = $17 \cdot 10^6$. As $c_l$ = 3.1 is achieved at $\alpha$ = 0°, all simulations have been conducted at this single angle of attack (AOA).

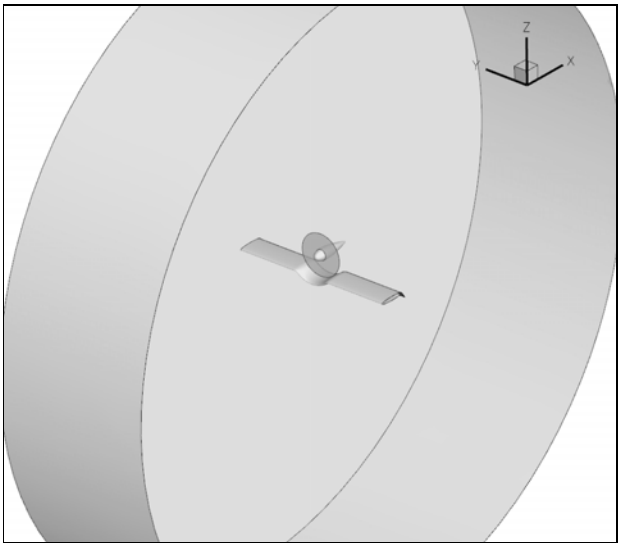


FIGURE 3. Geometry of the computational domain.

## 3. NUMERICAL SETUP

### 3.1. Grid

A cylindrical computational domain with a diameter of ten chord lengths (FIGURE 3) was selected to apply a symmetry condition on the side walls. All wing and nacelle surfaces were assigned a turbulent viscous wall condition. The unstructured grids were created by the commercial grid generator *Centaursoft Centaur* and contain approx. 15 million nodes. Grid sensitivity studies with three different sizes were performed for the 2D airfoil to reveal discretization error dependencies. Together with the requirement for the dimensionless wall distance of the first cell not to exceed $y^+$ = 1, a reasonable grid resolution was determined. In order to further improve the accuracy of the 3D solution, regions of expected high gradients like propeller slipstream and wake were refined by means of grid sources, see FIGURE 4.

### 3.2. Numerical Method

The steady CFD simulations were conducted by using the DLR TAU code for solving the RANS equations on the unstructured grids. Turbulence was modelled by the Spalart-Allmaras one-equation formulation [6] with a correction for rotational flow [7]. While the inviscid fluxes of the Navier-Stokes-Equations were discretized by a central scheme with scalar dissipation, the 2nd order upwind scheme by Roe was used for the convective fluxes of the turbulence equations. On the other hand, all viscous fluxes were discretized by a central scheme using a full gradient approach. A backward Euler relaxation solver was chosen to enable an implicit time integration scheme. The influence of laminar boundary layers on the aerodynamic properties was assumed to be negligibly small (Re = $17 \cdot 10^6$) so that all solid surfaces were treated fully turbulent.

### 3.3. Actuator Disk

The actuator disk model uses blade element theory to calculate the steady forces applied to the fluid [8]. This means that the actual inflow is taken into account which is particularly important for installed propellers in an inhomogeneous environment. According to the propeller design [9] which was done for a comparable application [10], the distribution of blade twist and chord length as well as the aerodynamic characteristics at discrete radii were prescribed. In practice, lift and drag over $\alpha$ was defined for five blade profile sections and a reasonable range including stall behaviour. Compared to the original propeller design, the propeller was scaled to fit the requirements of the STOL aircraft concept. The number of blades, nine, rotational speed (975 rpm) and pitch angle had to be specified as well.

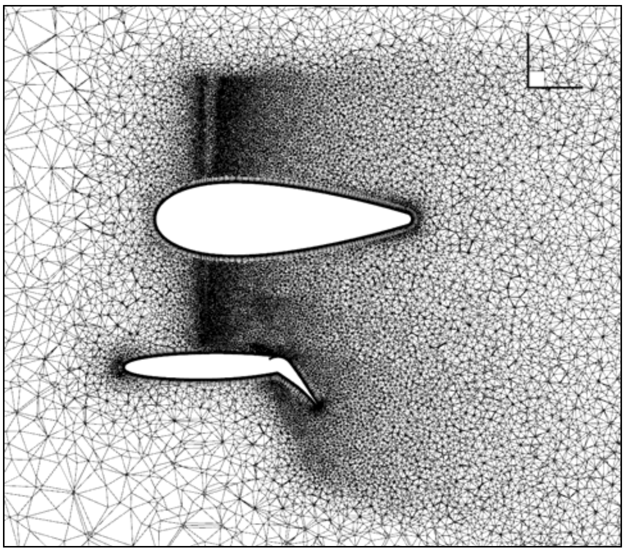

FIGURE 4. Midspan cross section of 3D mesh showing the effect of source-based refinements.

## 4. RESULTS

### 4.1. Influence of Embedding Depth

Before analyzing the effects of changing the propeller position in the channel, the impact of its embedding depth on the aerodynamics of such a configuration is discussed. This parameter can be also replaced by the aerodynamically more relevant azimuth angle or spanwise extent. The impact of the wing on the propeller distributions is only discussed for the channel depth variations as this parameter has a very distinct influence on the actuator inflow.

#### 4.1.1. Propeller Distributions

It is shown in [2] that an over-the-wing propeller suffers from inhomogeneous inflow conditions, particularly a vertical gradient of the axial velocity. Even when adjusting the blade pitch angle to achieve the shaft power of an isolated rotor

$$C_{P,s} = \frac{P_S}{\rho_\infty D_P^5 n^3} = 0.457\,, \tag{3}$$

the effective blade AOA and local thrust decrease (cf. FIGURE 5). Hence, the net thrust and therefore propeller efficiency

$$\eta_P = \frac{T \cdot V_\infty}{P_S} \tag{4}$$

are reduced by a certain amount.

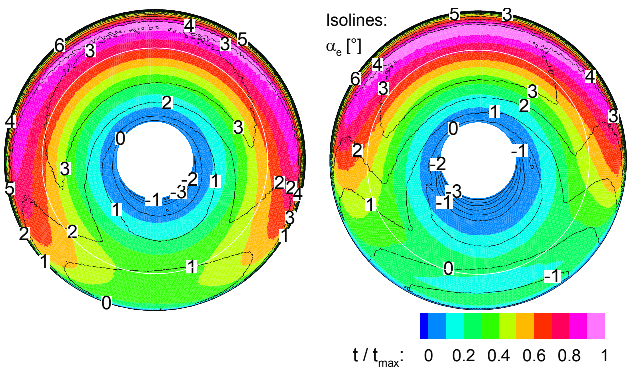


(a) Zero channel depth, $C_T = 0.659$

(b) Channel depth of 1/2 $D_P$ $C_T = 0.588$

FIGURE 5. Distributions of effective blade AOA $\alpha_e$ and relative thrust $t/t_{max}$ at constant shaft power coefficient $C_{P,s} = 0.457$.

As the non-embedded propeller is operating in a spanwisely constant flow gradient pointing in z-direction, a corresponding gradient of $t/t_{max}$ is induced on the disk. In contrast, the half-barrel channel wing ($\Delta z_P/D_P = 0.5$) changes the inflow velocity profile in the complete lower half of the propeller in a radial manner. In other words, the direction of the velocity gradient is pointing to the rotor axis. Such a maximum integrated channel wing propeller loses another 11 % of thrust when compared to the plain over-the-wing propeller.

#### 4.1.2. Chordwise and Spanwise Distributions

The general effect of propeller installation on wing aerodynamics and coefficients can be found in [2]. Looking at the pressure distribution at the midspan section (location of the propeller axis) of the wing, FIGURE 6, all over-the-wing propeller configurations show a significantly increased and extended suction peak near the leading edge. Depending on the channel depth, the rear suction peak is amplified due to the slipstream and for $\Delta z_P/D_P = 0.5$ reaches the level of a tractor configuration. Although the cross section geometry, particularly the gap between propeller disk and upper wing surface is identical for all channel geometries, the pressure level on the upper surface is directly influenced by the spanwise extent of integration. As a result, the fully embedded propeller induces a significantly higher lift gain on this section of the wing than a less integrated configuration such as the plain overwing. Only the magnitude of the LE suction peak and the lower surface distribution are independent of the embedding depth.

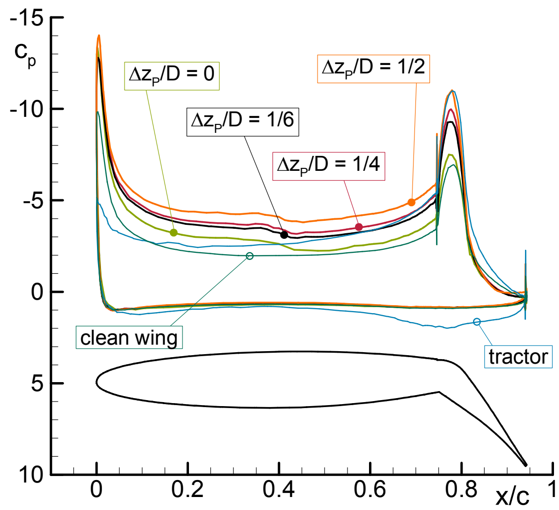


FIGURE 6. Pressure coefficient distribution at midspan for different channel depths.

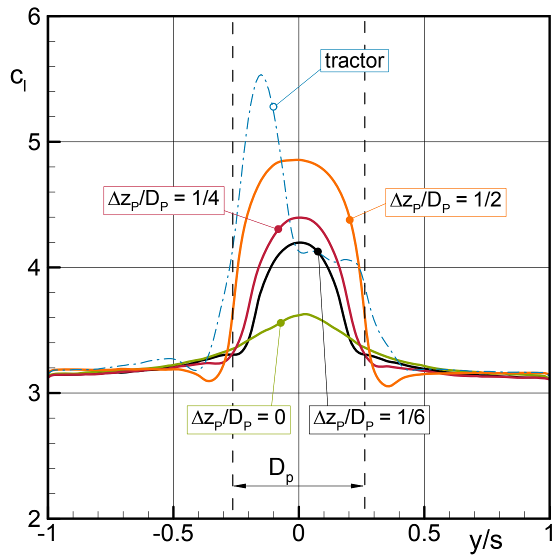


FIGURE 7. Spanwise distribution of the lift coefficient for different channel depths.

It is not surprising that similar trends can be found for the spanwise distribution of lift coefficient, see FIGURE 7. Starting from the lift maximum near the propeller axis, the lift coefficients drop down to asymptotically reach the value of the isolated airfoil of $c_l$ = 3.1. However, the shape differs from case to case. The steepest slope is always found near the channel. Note that the tractor configuration produces a strong asymmetry due to the swirl in the propeller wake, while the over-the-wing installation leads to an almost symmetric variation of the lift coefficient.

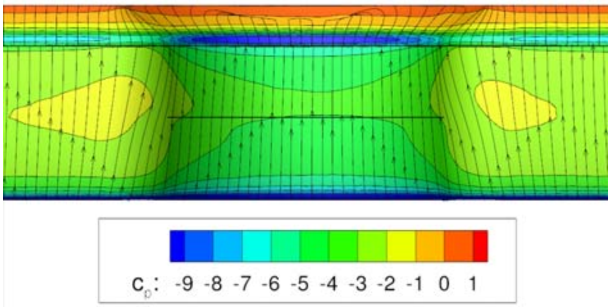


FIGURE 8. Top view of the upper surface ($\Delta z_P/D_P$ = 0.5) showing wall stream lines and the pressure coefficient distribution.

An effect that is particularly visible for the fully embedded propeller is the local lift minimum at the rounded edge of the channel. The surface pressure coefficients in FIGURE 8 indicate a weak suction peak at the Coanda surface of the corresponding regions which also affect the pressure level of the whole upper surface. Actually the jet momentum coefficient $c_\mu$ between the channel and outer wing is lowered by 8 % although the total pressure in the plenum is spanwisely constant. The reason is that the jet is converging on the triangle-shaped flap and thus increasing in thickness which reduces the blowing efficiency. It is assumed that the crossflow on the surface which is dominant at the edge of the channel may also influence the pressure distribution.

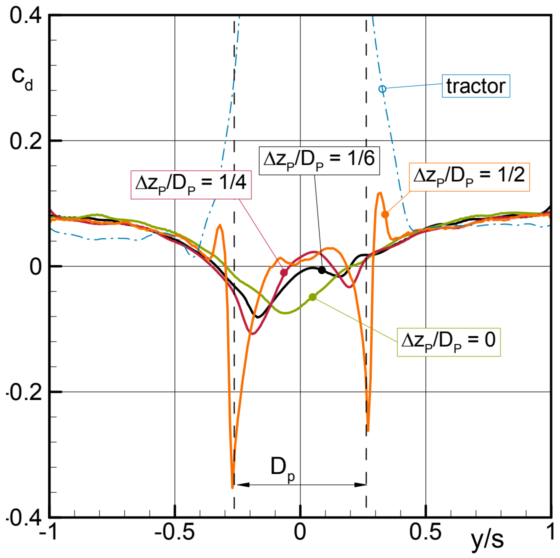


FIGURE 9. Spanwise distribution of the drag coefficient for different channel depths.

Looking at the distribution of the drag coefficient (FIGURE 9) it is evident that all over-the-wing configurations lead to a decrease in drag over a large portion of the span in contrast to a tractor propeller. Moreover, induced thrust can be observed in some regions with $c_d$ < 0. This is particularly true for the non-embedded propeller near midspan which shows a symmetric and smooth distribution. Things are different for the channel wing where the minimum drag (or maximum thrust) can be found at the channel edge radius whereas a local maximum occurs at the midspan section. The configuration with maximum channel depth shows again extreme local values and gradients together with overshoots in the transition area between outer wing and channel. While the lift coefficient is almost symmetrically distributed along the span the drag coefficient is much more sensitive to propeller swirl effects, namely up- and downwash velocities induced on the rear part of the wing.

### 4.1.3. Overall Perfomance

In coherence with [2], the aerodynamic performance of the overall configuration is assessed by a balance of forces with regard to a preliminary aircraft design. The approach is the following:

1. Determination of the difference between the actual spanwise coefficient and value of the isolated airfoil to obtain the pure propeller effect, e.g. $\Delta c_l = c_l - 3.1$.

2. Integration along a representative span segment $\Delta y = b/2$ (around the propeller axis) to extract the propulsion-induced force differences on this wing. These forces $\Delta L$ and $\Delta D$ are approximately valid for the aircraft design as the wing section most influenced by the propeller is similar to the CFD geometry.

3. Relating the forces including thrust on the aircraft domain by multiplying with two (number of engines) and normalizing with the dynamic pressure $q_\infty$ and wing area $S_{ref}$. The thrust coefficient for the aircraft is

   $$(5)\quad C_T = \frac{2 \cdot T}{q_\infty S_{ref}}.$$

   Note that for a fair comparison the power coefficient $C_P$ has always kept constant. The lift increment due to the propeller is

   $$(6)\quad \Delta C_L = \frac{2 \cdot \Delta L}{q_\infty S_{ref}}.$$

4. Definition of two figures of merit which are adapted to the mutual influence of propeller and wing.

   (a) The common propeller efficiency $\eta_P$ is converted into the propulsive efficiency $\eta_{Pro}$ by using the installed thrust of the configuration $T_{inst} = T - \Delta D$, cf. equation (4).

   (b) The lift-to-drag ratio $L/D$ is corrected by the thrust loss coefficient on the actuator disk $\Delta C_T = C_{T,isol} - C_T$ to get

   $$(7)\quad \frac{L}{D^*} = \frac{C_L}{C_D^*} = \frac{C_{L,ref} + \Delta C_L}{C_{D,ref} + \Delta C_D + \Delta C_T}.$$

   The absolute lift and drag coefficients ($C_{L,ref}$, $C_{D,ref}$) are obtained from preliminary design data of the reference aircraft at take-off.

First, FIGURE 10 shows the development of the lift increment $\Delta C_L$ over the channel depth. As indicated by the pressure and particularly the spanwise lift distributions, $\Delta C_L$ can be enhanced significantly through maximum propeller embedding. A nearly linear correlation is evident when using the actual parameter of channel depth. Looking at the *L/D*-dependencies, it is striking that judging on the conventional definition may lead to a wrong conclusion as the corrected figure shows a reverse trend. In fact, the lift-to-drag ratio of the configuration *L/D** is almost constant for the channel wing and slightly higher for the plain over-wing design. Due to the favourable lift augmentation, a half-barrel ($\Delta z_P/D_P$ = 0.5) channel wing is a good choice for high-lift at this operating point resp. AOA.

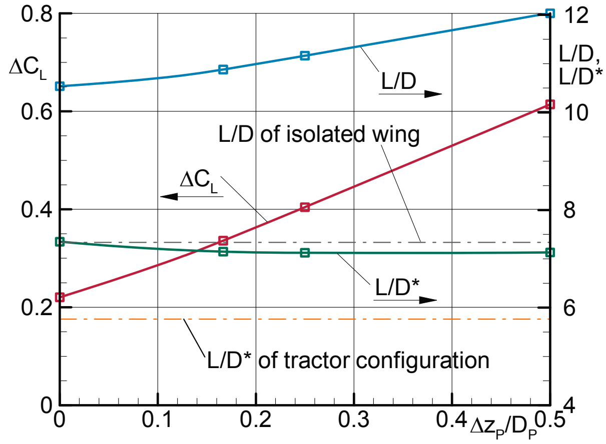


FIGURE 10. Lift gain and lift-to-drag ratio as functions of the channel depth.

This statement must be qualified when looking at the axial balance with the installed thrust at given shaft power as outcome, see FIGURE 11. The corresponding propulsive efficiency $\eta_{Pro}$ decreases nearly linearly with increasing channel depth with a maximum difference of $\eta_{Pro}$ = 0.05 or 9%. As the propeller efficiency has a constant offset, the progressive trust loss on the actuator disk due to in homogeneities is the main driver for this behaviour. An assessment on the basis of aerodynamic quality in terms of *L/D** and $\eta_{Pro}$ indicates an advantage for non-embedded over-the-wing propellers although the reachable lift-gain of $\Delta C_L$ = 0.2 is comparatively small. It shall be noted that this configuration, on the other hand, shows an unfavourable nose-down pitching moment due to thrust as the propeller axis has the largest distance to the centre of gravity [2].

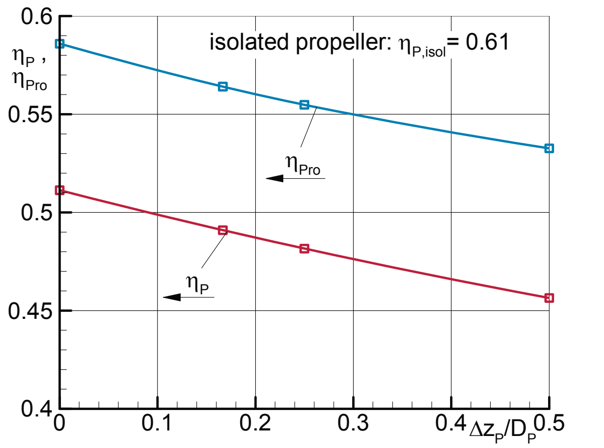


FIGURE 11. Propeller and propulsive efficiencies as functions of the channel depth.

## 4.2. Influence of Chordwise Position

### 4.2.1. Chordwise and Spanwise Distributions

As shown by FIGURE 12 for the midspan cross section, the axial position of the propeller has limited influence on the pressure distribution. In particular, the region of amplified suction pressure upstream of the propeller is extended to its actual position. Hence, a longer suction peak and thus higher lift gain is achieved by the rear actuator disk location. However, the size of the suction peak on the Coanda surface is surprisingly independent of $x_P/c$. It is furthermore striking that the foremost propeller position leads to stall, see FIGURE 12, blue line. In fact, the boundary layer is still attached, at least at midspan, while the outer flow shows a recirculation area above the flap (FIGURE 13). Most likely, the additional, abrupt pressure rise due to the actuator disk at the end of the suction peak weakens the boundary layer which consequently cannot follow the deflected flap. This is the typical stall appearance for this kind of IBF-wing which occurs at a small AOA when no leading edge device is applied [4]. Further work has to include the dependency of $x_P/c$ on $\alpha_{max}$ which is particularly important for an assessment of the landing performance.

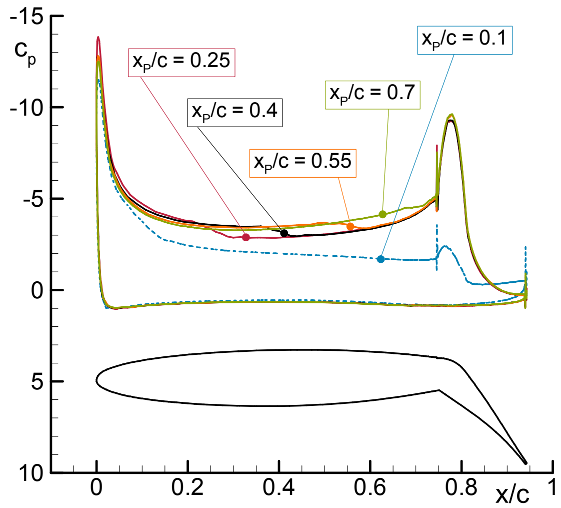


FIGURE 12. Pressure distribution at midspan for different channel depths.

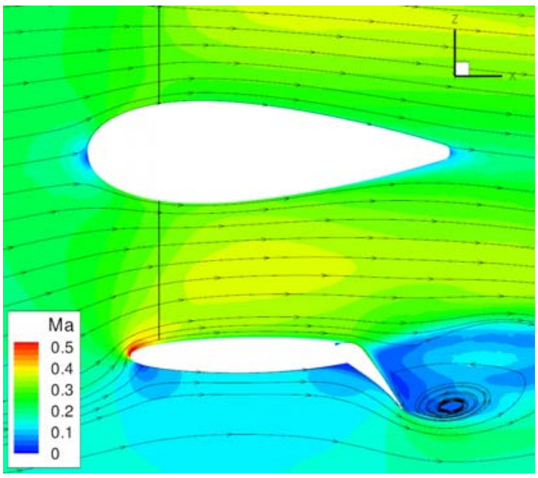


FIGURE 13. Midspan flow field in terms of Mach number distribution and streamlines for $x_P/c$=*0.1.*

As can be seen in FIGURE 12, the propeller lowers the pressure in front of the propeller, therefore increasing lift. On the other hand it also affects the suction peak and the shape of the pressure recovery region immediately following the peak. The combination of both effects leads to a slow increase of lift with a downstream shift of the propeller, cf. FIGURE 14. A closer look at the pressure distribution reveals that the distinct gain upstream of the rear location is nearly compensated by the slightly different $c_p$-level from the leading edge to the forward propeller location.

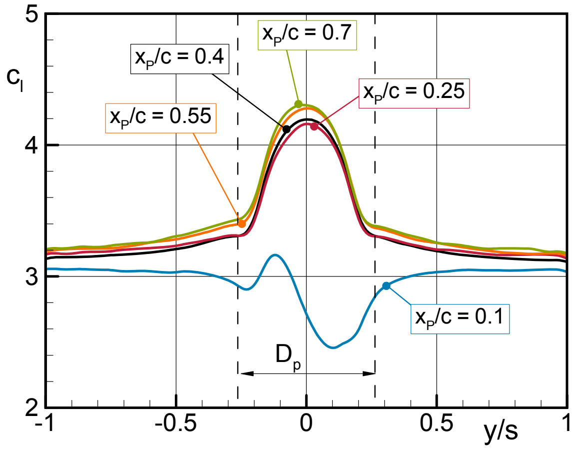


FIGURE 14. Spanwise distribution of the lift coefficient for different chordwise propeller positions.

As the additional lift is shifted further downstream depending on $x_P/c$, pressure drag is increased due to the local surface orientation and thus backward pointing pressure forces. Also the lower suction pressures in the pressure recovery region behind the suction peak produced by the more downstream propeller locations reduce the suction force in the forward portion of the wing. Very low drag and high induced thrust, respectively, is achieved for the configuration with foremost propeller position ($x_P/c$ = 0.25, FIGURE 15) while the stalled test case is not considered.

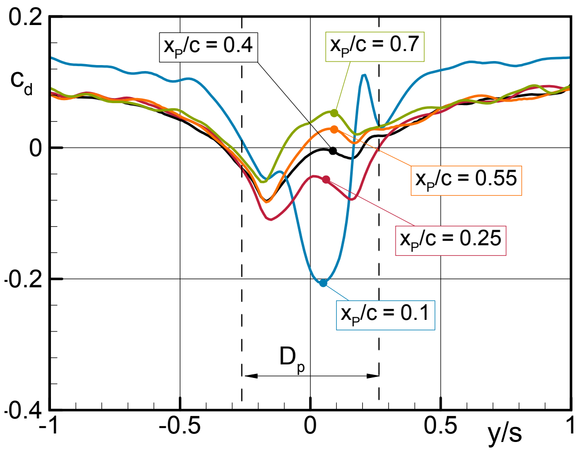


FIGURE 15. Spanwise distribution of the drag coefficient for different chordwise propeller positions.

#### 4.2.2. Overall Performance

As indicated by the spanwise distributions, the lift gain $\Delta C_L$ is apparently nonlinear with $x_P/c$ whereas the steepest slope can be found at midchord, see FIGURE 16. The reverse trend is evident for both lift-to-drag ratio definitions. For this figure of merit, a nearly constant gradient is found from $x_P/c$ = 0.4 to 0.55 which means that additional lift can be gained by placing the propeller backwards without any drawbacks. It is obvious that the drag increment is then higher which accordingly reduces the installed thrust and propulsive efficiency, respectively. In fact, $\eta_{Pro}$ decreases nearly linearly with increasing propeller coordinate while the propeller performance in terms of $\eta_P$ is not sensitive to the axial position (cf. FIGURE 17). Despite the moderate lift gain capabilities, the propeller at 25 % chord length is identified as aerodynamic optimum. Another favourable configuration is the $x_P/c$ = 0.55 version which delivers highest $C_L$-augmentation at acceptable figures of merit.

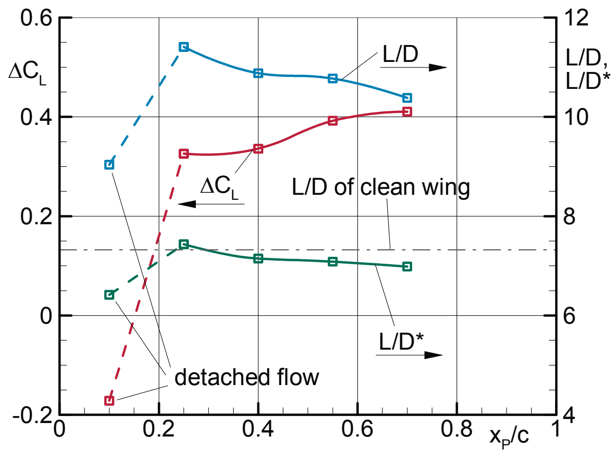


FIGURE 16. Lift gain and lift-to-drag ratio as functions of the chordwise propeller position.

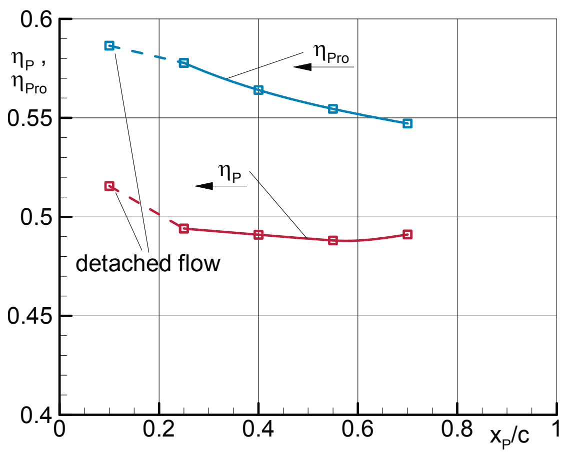


FIGURE 17. Propeller and propulsive efficiencies as functions of the chordwise propeller position.

### 4.3. Influence of Clearance

#### 4.3.1. Chordwise and Spanwise Distributions

Looking at FIGURE 18 it is striking that the variation of the gap between rotor tip and wing surface has little effect on the pressure distribution. Only the academically small clearance of 0.2 % (which means a distance of 1 cm for a propeller with a diameter of 5 m) shows some amplification at the rear suction peak. Apparently, the propeller has to penetrate the boundary layer, which is approximately 1 % of $D_P$ thick at this location, to have a significant effect on the pressure distribution. The fact that most of the thrust on the actuator disk is generated far away from the wing apparently leads to this kind of sensitivity for the potential flow as the variation is small in relation to the diameter of the propeller.

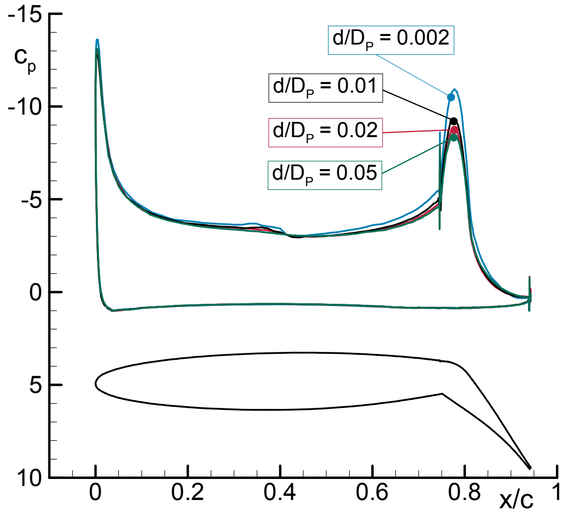


FIGURE 18. Distribution of the pressure coefficient at midspan for different clearances.

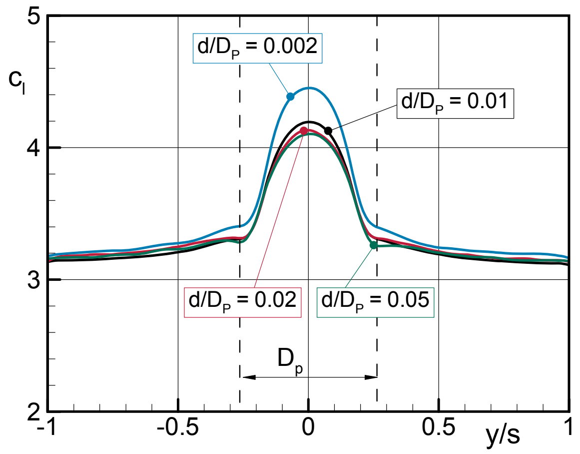


FIGURE 19. Spanwise distribution of the lift coefficient for different clearances.

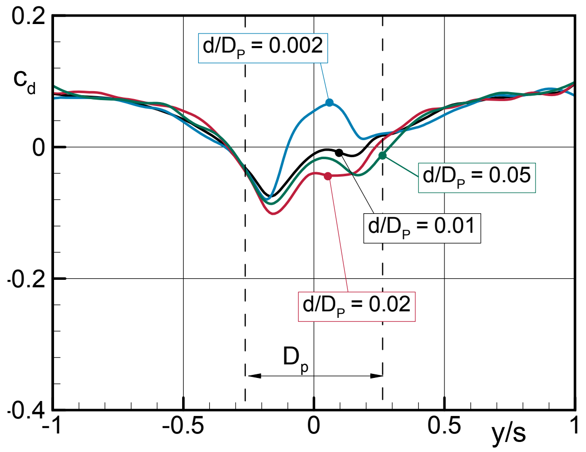


FIGURE 20. Spanwise distribution of the drag coefficient for different clearances.

The spanwise lift and drag distributions (FIGURE 19 and FIGURE 20) show an accordingly small impact when increasing the distance from 1 % to 5 % of $D_P$. In contrast, the lift gain and drag rise are comparatively large for the smallest gap which was not expected from the pressure distribution. It is worth mentioning that a clearance less than $d/D_P$ =1 % is likely not feasible concerning manufacturing and operation.

### 4.3.2. Overall Performance

Having in mind the spanwise distributions of lift and drag, it is obvious that the configurations between $d/D_P$ = 0.01 and 0.05 are performing quite similar, see FIGURE 21. However, due to the lower drag, an advantage can be identified for the larger clearance as $L/D^*$ and $\eta_{Pro}$ are enhanced to some degree. Only the minimum gap approach ($d/D_P$ = 0.002) delivers significantly more $\Delta C_L$ but also more drag which leads to a comparable lift-to drag ratio at reduced propulsive efficiency. As evident from the propeller efficiency curve ($\eta_P$ vs. $d/D_P$, FIGURE 22), the net thrust and thus inhomogeneity at the propeller is not influenced by the gap size.

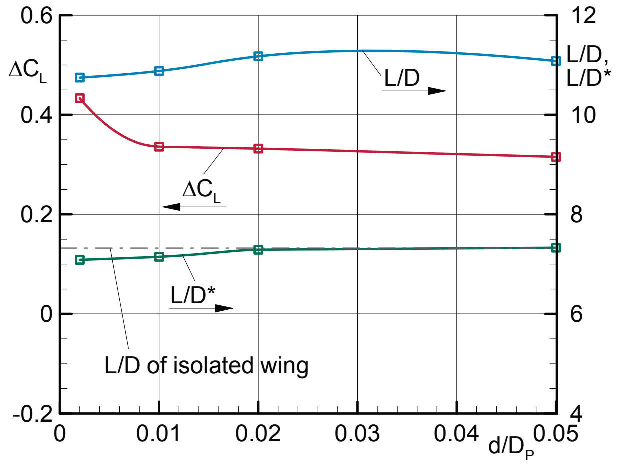


FIGURE 21. Lift gain and lift-to-drag ratio as functions of clearance.

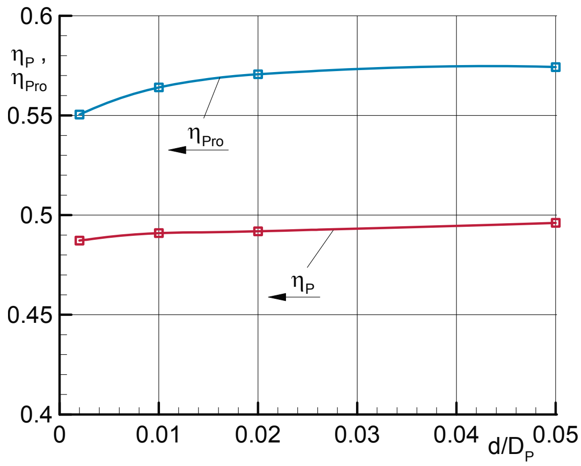


FIGURE 22. Propeller and propulsive efficiencies as functions of clearance.

## 5. CONCLUSIONS AND OUTLOOK

The channel depth, the axial position and the clearance of the propeller have various impacts on propeller and wing aerodynamics. To allow for reasonable assessment, the wing-related lift-to-drag ratio *L/D*, the propeller efficiency $\eta_P$ and a thrust-weighted lift-to-drag ratio for the overall configuration *L/D** have been calculated. In addition, the vertical and axial balance of forces are represented by the lift increment $\Delta C_L$ and propulsive efficiency, respectively. First, the two single components, namely the wing and the propeller are discussed regarding the particular trends of their figures of merit *L/D* and $\eta_P$, respectively:

- By increasing the channel depth, the lift-to-drag ratio increases from 10.5 to 12 while the propeller efficiency linearly decreases by $\Delta\eta_P = 0.05$.

- While the axial location of the propeller has hardly any impact on $\eta_P$, a front position has a positive influence on *L/D* as the drag is significantly reduced. Based on the spacing of this study, the propeller position is restricted to coordinates larger or equal to $x_P/c = 0.25$ due to the tendency to stall at lower values. This means that the aerodynamic optimum can be found at the foremost position which fulfils the required stall margin.

- Although a small clearance amplifies the integration effects such as lift augmentation, both figures of merit are consistently enhanced by a large gap size. This is not surprising as it was shown that a fully isolated case is superior to channel wing and plain overwing configurations [2].

Despite these complex dependencies, the essential figure of merit concerning the overall configuration, *L/D**, is almost not influenced by any of the geometry parameters. This can be interpreted as an advantage when considering the robustness of wing design. More specifically, an optimum solution can be found in terms structure, aeroacoustics and flight dynamics without serious aerodynamic restrictions (except for the stalled case $x_P/c = 0.1$). However, the aerodynamic optimum is a plain overwing (non-embedded, $\Delta z_P/D_P = 0$) configuration with maximum clearance ($d/D_P = 2\,\%$) and a propeller at an axial position of $x_P/c = 0.25$.

Future work will include the variation of geometry details and three-dimensional wing shapes, cruise conditions at higher Mach numbers with retracted flap as well as optimized (adaptive) propeller design to exploit the potential of channel wing configurations. Apart from these actuator disk simulations, unsteady RANS computations with full propeller geometry will give an insight into the flow phenomena of such interaction.

## 6. ACKNOWLEDGEMENTS

This work was funded by the Deutsche Forschungsgemeinschaft DFG (German Research Funding Organisation) in the framework of the collaborative research centre SFB 880. The authors would like to acknowledge Axel Raichle, DLR Braunschweig, Institute of Aerodynamics and Flow Technology for his support regarding the actuator disc model in TAU. Further thanks go to Carsten Lenfers (DLR) for providing propeller data and Jochen Wild (DLR) for providing the wing airfoil geometry. We would also like to acknowledge Wolfgang Heinze of the Institute of Aircraft Design and Lightweight Structures, TU Braunschweig for his multidisciplinary studies on the STOL aircraft in SFB 880.

## REFERENCES


[1] Airbus S.A.S., „Delivering the Future“, *Global Market Forecast 2011-2030*, Blagnac, France, 2011.

[2] L. Müller, D. Kozulovic, M. Hepperle, R. Radespiel, „Installation Effects of a Propeller Over a Wing with Internally Blown Flaps“, *Proceedings of the 30th AIAA Applied Aerodynamics Conference*, Paper AIAA 2012-3335, New Orleans, LA (USA) 2012.

[3] J. Wild, G. Wichmann, F. Haucke, I. Peltzer, and P. Scholz, “Large scale separation flow control experiments within the German Flow Control Network”, *Proceedings of the 47th AIAA Aerospace Sciences Meeting*, Paper No. AIAA 2009-0530, Orlando, FL (USA)

[4] C. Jensch, K.-C. Pfingsten, R. Radespiel, M. Schuermann, M. Haupt, and S. Bauss, “Design Aspects of a Gapless High-Lift System with Active Blowing”, *Proceedings of Deutscher Luft- und Raumfahrtkongress 2009*, Aachen, Germany, 2009.

[5] N. Beck, M. Wentrup, and R. Radespiel, “Realisierung eines Windkanalexperiments für aktiven Hochauftrieb”, *Proceedings of Deutscher Luft- und Raumfahrtkongress 2011*, Bremen, Germany, 2011.

[6] P. R. Spalart and S. R. Allmaras, “A One-Equation Turbulence Model for Aerodynamic Flows,” AIAA Paper, No. 92-0439, 1992.

[7] M. L. Shur, M. Strelets, A. K. Travin, and P. R. Spalart, “Turbulence Modeling in Rotating and Curved Channels: Assessing the Spalart-Shur Correction,” AIAA Journal, Vol. 38, No. 5, pp. 784-792, 2000.

[8] A. Raichle, S. Melber-Wilkening, and J. Himisch, “A New Actuator Disk Model for the TAU Code and Application to a Sailplane with a Folding Engine,” *Proceedings of the 15th STAB/DGLR Symposium*, Darmstadt, Germany, 2006.

[9] C. Lenfers, “Propeller Design for a future QESTOL Aircraft in the BNF Project”, *Proceedings of the 30th AIAA Applied Aerodynamics Conference*, Paper AIAA 2012-3334, New Orleans, LA (USA) 2012.

[10] C. Butzmühlen and P. Hecker, “Das Bürgernahe Flugzeug”, *Proceedings of Deutscher Luft- und Raumfahrtkongress 2010*, Hamburg, Germany, 2010.